



Implementation of Remote Sensing Techniques in Structural and Lithological Mapping of Northwestern Margin of Red Sea, Egypt

Farouk Sayed^{1*}, Mohamed S. Hammed², Ahmed G. Shided¹ and Ahmed W. Hussein¹

1. Geology Department, Faculty of Science, Fayoum University, Egypt

2. Geology Department, Faculty of Science, Cairo University, Egypt

Article Info

Received 21 January 2023

Received in Revised form 28
February 2023

Accepted 18 March 2023

Published online 18 March 2023

[DOI:10.22044/jme.2023.12628.2294](https://doi.org/10.22044/jme.2023.12628.2294)

Keywords

Landsat-8 (OLI)

PALSAR

Remote sensing techniques

Structural mapping

Red Sea

Abstract

The northwestern margin of the Red Sea is developed as several rift-related fault blocks. These fault blocks comprise two mega tectono-stratigraphic successions; the Pre-rift succession could be sub-divided into the Precambrian Basement rocks and the Upper Cretaceous-Lower Eocene deposits, whilst the Syn-rift sequence includes the Oligocene to Quaternary deposits. Lithologic differentiation of these rock units being encountered in the studied area is accomplished utilizing different remote sensing imagery enhancement techniques of the OLI data (Landsat-8) aided with field verification. Spectral signature analysis of different rock units, false-color composite, band-ratio, principle component analysis, minimum noise fraction, and independent component analysis are powerful tools in discrimination of the main rock units. The maximum likelihood distance supervised classification technique is a robust tool in the identification of the contact between the different rock units. Radiometrically terrain corrected (RTC) DEM data extracted from PALSAR with a spatial resolution of 12.5m is utilized for the construction of a 3D perspective view image of the studied area. The present study offers a unique method for lithologic discrimination of main rock units utilizing OLI images, and introduces an enhanced high-resolution structural map of the studied area aided with field verification.

1. Introduction

The accelerated development rate of satellite imagery and remote sensing techniques during the last decades supplies intensified data about the geomorphologic, lithologic, and structural characteristics of the surface of the earth. Remote sensing applications are widely utilized for the discrimination of lithological units, mapping of structural elements, and mineral prospecting, (e.g. [1-11] and others). Landsat-8 mission commenced on 2013. It is composed of two passive sensors (Table 1); the **Operational Land Imager (OLI)** supplies seasonal coverage of the global landmass. It is composed of nine bands (including visible, NIR, SWIR and cirrus bands with 30 m spatial resolution and a panchromatic band with a finer spatial resolution of 15 m, in addition to the **Thermal Infrared Sensor (TIRS)** with two thermal bands with 100 meters spatial

resolution. The Landsat-8 images have been vastly utilized in lithological discrimination and structure mapping ([11-26] and others). During the last years, the Red Sea environs entice the consideration of many geologists due to the several oil and minerals exploration and prospecting programs that have been constructed through the Red Sea district. The study territory is situated at the northern sector of the Red Sea of Egypt (Figure 1 (a)); covering a surface area of about 4200 Km² between longitudes of 33°34'58.26" to 34°31'13.97" E and latitudes of 25°42'2.39" to 26°38'35.73" N. The purpose of the existing work is to integrate the results of the remote-sensing techniques obtained from the OLI data with the field verification to differentiate the different rock units and construct an enhanced detailed structural mapping of the studied territory.

✉ Corresponding author: Fsm00@fayoum.edu.eg (F. Sayed)

Table 1. Sensor characteristics of Landsat 8.

Wavelength Region	Band No.	Spectral resolution (μm)	Spatial resolution (m)
Visible / Near Infra- red	Band No.1	0.43-0.45	30
	Band No.2	0.45-0.51	
	Band No.3	0.53-0.59	
	Band No.4	0.64-0.67	
	Band No.5	0.85-0.88	
Short Wave Infra-red	Band No.6	1.57-1.65	30
	Band No.7	2.11-2.29	
Panchromatic	Band No.8	0.50-0.68	15
Cirrus	Band No.9	1.363-1.384	30
Thermal Infra-red	Band No.10	10.62-11.19	100
	Band No.11	11.50-12.51	

2. Geologic Setting

The study precinct represents the NW segment of the Red Sea successful rift basin. It comprises several rift-related faulted-blocks, e.g. Gebel Duwi, Gebel Hamadat and Zug El-Bohar (Figure 1 (a)). Two main tectono-stratigraphic megasequences are associated with the Red Sea rift system (Figure 1 (b)), namely: 1) The pre-rift succession is composed of the Precambrian basement rocks in addition to the Upper Cretaceous to Lower Eocene sedimentary succession, and 2) The syn-rift sequence, represented by the Oligocene to Recent sedimentary succession.

The Late Precambrian (Neoproterozoic) Pan-African Basement rocks [27-32] of the studied area is represented by seven rock units; Metavolcanics (Figure 2 (a, c, and f)), Metasediments (Figure 2 (a and d)), Metagabbro-diorite (Figure 2 (b)), Dokhan volcanics, Hammamat sediments (Figure 2 (c)), younger granite (Figure 2 (d and e)) and Post Hammamat felsite. The Pre-rift sedimentary rock units comprise mixed clastic and carbonate rocks rest nonconformably overlying the Precambrian rocks (Figure 2 (f)). They are ranging from the Upper Cretaceous to Lower Eocene (Figure 1 (b)), and could be sub-divided into the following rock units. The oldest exposed sedimentary rocks are characterized by cross-bedded sandstone and conglomeratic sandstone of the Turonian to Santonian named the Nubian Sandstone [33]. The Nubian Sandstone is overlain by shales and marl of the Campanian Quseir Shale [34-36]. The Quseir shale is overlain by shale, marl and carbonate with several phosphate interbeds of the Upper Campanian to Maastrichtian Duwi Formation [33] (Figure 2 (g)). The Duwi Formation is overlain by the Maastrichtian -Lower Paleocene Dakhla Shale which is composed mainly of shale and marl [37-40]. The Upper Paleocene marly limestone of the Tarawan Chalk [33] conformably overlies the

Dakhla Shale (Figure 2 (h)). The Tarawan Chalk is conformably superimposed by the Esna Shale of Paleocene-Lower Eocene age [33]. The youngest exposed pre-rift deposits are represented by cliff-forming rigid limestone of the Lower Eocene Thebes Formation [37]. The Pre-rift rock units constitute the main outcrops of the rift-related fault blocks (Figure 2 (i)).

The deposits of the Syn-rift sequence are structurally controlled and occupy structurally developed lowlands [41] and could be subdivided (from older to younger) into the following rock units. The oldest recorded deposits are the conglomerate (composed of reworked limestone fragments of the Thebes Formation) and lacustrine carbonate of the Oligocene Nakheil Formation (Figure 2 (j)) [42]. The Oligocene deposits in the southern sector of the studied area are represented by ferruginated sandstone with basal conglomerate named the Abu-Ghusun Formation [43 and 44] and covered by basaltic flows at parts (Figure 2 (k)) [45]. The Lower Miocene fan-related conglomerate and sandstone deposits are named the Ranga Formation (Figure 2 (l)) [46 and 47]. The Ranga Formation is conformably overlain by the Middle Miocene fine clastics and reefal limestone of the Um Mahara Formation (Figure 2 (m)). The Um Mahara Formation is unconformably overlying older rock units at parts (Figure 2 (b and e)) [44 and 47]. The Middle to Upper Miocene Abu-Dabbab Formation is built up of evaporite-dominated facies [48] with shale interbeds with brain-like weathering geometry. The Abu-Dabbab Formation is overlain by the Pliocene clastics of the Marsa Alam Formation (Figure 2 (n)). The clastic-dominated facies of Marsa Alam Formation is overlain by patchy appearance reefal limestone facies of the Shagara Formation [33]. The Youngest exposed deposits are represented by the Quaternary alluvial fans and raised corals.

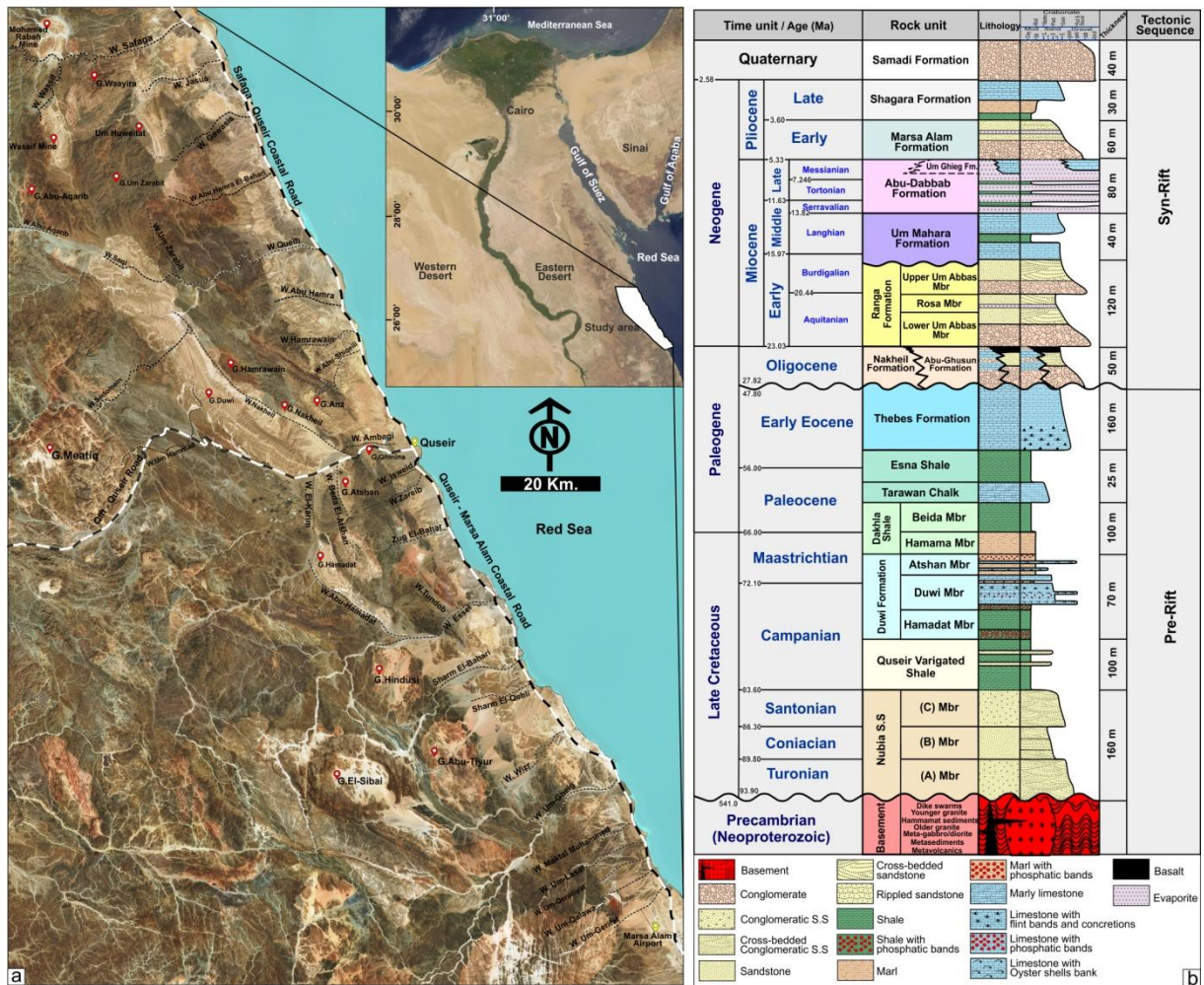


Figure 1. a. Location map and Google Earth image shows the Physiography of the studied area, b. Stratigraphic column of the studied area (Modified after Khalil and McClay, 2002).

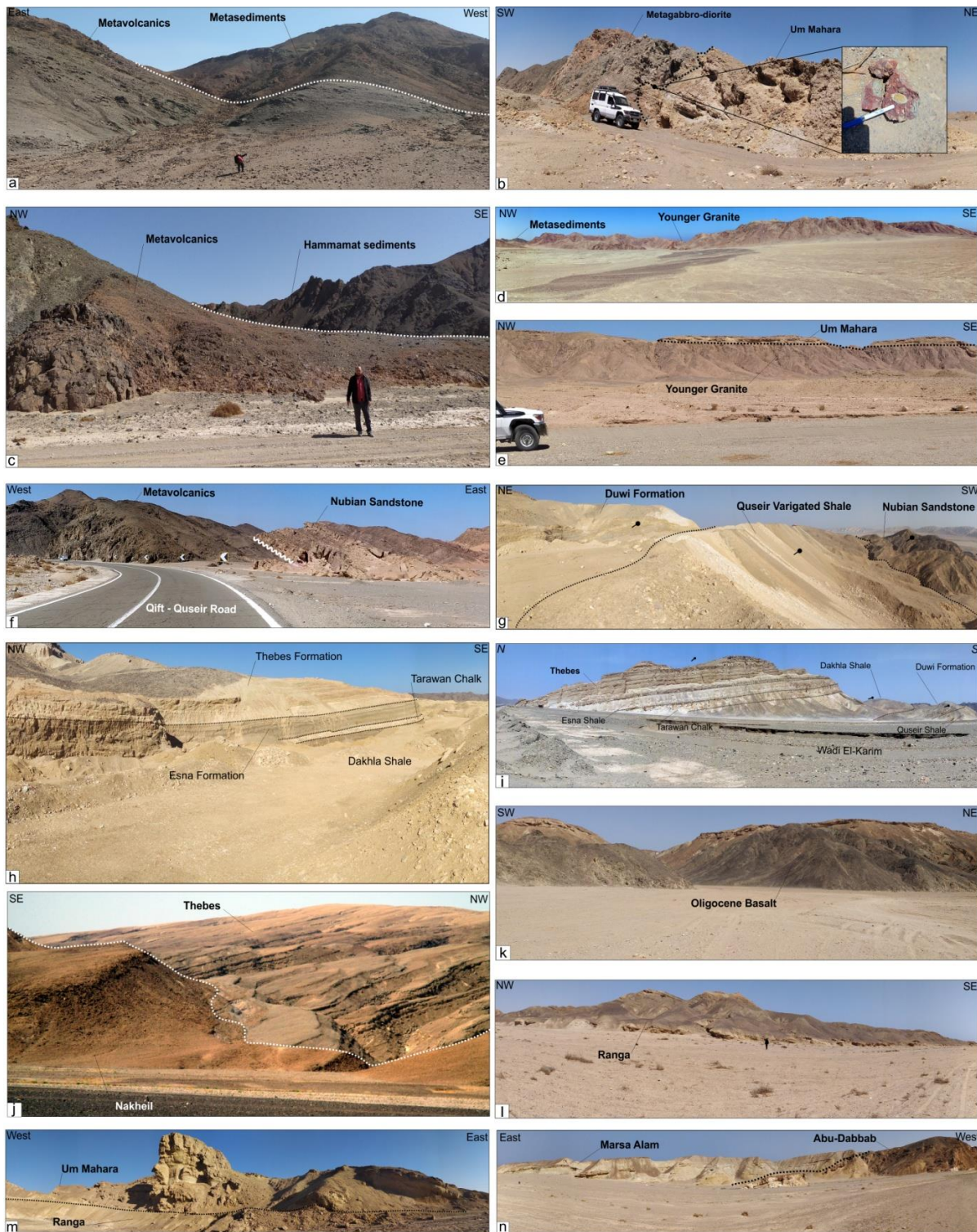


Figure 2. Field Photographs showing: a. Contact between the Metavolcanics and the Metasediments, Zug El-Bohar, b. Reefal limestone of the Um Mahara Formation nonconformably overlapped on the Metagabbro-diorite, Notice presence of Lead-Zinc mineralization along contact, Zug El-Bohar; c. Contact between the Metavolcanics and the Hammamat Sediments, Wadi Essel; d. Contact between the Younger Granite and the Metasediments, Wadi Tundub; e. Reefal limestone of the Um Mahara Formation nonconformably overlying the Younger Granite, Wadi Tundub; f. Nonconformity surface between the Precambrian basement (Metavolcanics) and the Nubian Sandstone, Gebel Duwi, Qift-Quseir Road; g. Pre-rift deposits of the Nubian Sandstone, Quseir and Duwi formations at Gebel Anz syncline; h. Conformable stratigraphic contact of the Dakhla Shale, Tarawan Chalk, Esna Shale and Thebes formation, Gebel Hamadat; i. The main outcrop of the NE-dipping limb of the Gebel Rewagen syncline (Quseir, Duwi, Dakhla, Tarawan, Esna, Thebes formations); j. Unconformable stratigraphic contact between Oligocene Nakheil and Thebes Formations, Gebel Duwi; k. Oligocene basaltic flow, Sharm El-Bahari; l. Gilberte type fan delta of the Ranga Formation, Sharm El-Bahari; m. Conformable stratigraphic contact between the Ranga Formation and the Um Mahara Formation, Zug El-Bohar; and n. Stratigraphic contact between the Abu-Dabbab Formation and Pliocene clastics of the Marsa Alam Formation, Wadi Wizr.

3. Dataset and Methodology

The present study utilizes different remote sensing images including the following data set;

- a) Visual interpretation of Google Earth images in addition to the previous techniques used for precise rock discrimination (e.g. color, texture, pattern, and geometry).
- b) One Landsat 8 scene of path 174 / row 042 covered the studied area, and was acquired in August 2018 with scene ID LC81740422018231LGN00. It was downloaded from the Glovis website (glovis.usgs.gov), which is related to the US Geological Survey (USGS). This scene has been georeferenced to Zone 36 N of the UTM projection and WGS-84 datum. It has been corrected from instrumental and geometrical errors. Atmospheric correction of the scene utilizing FLAASH (Fast Line of Sight Atmospheric Analysis of Spectral Hypercube) has been performed, then has been resampled. Several digital remote sensing enhancement techniques have been applied for this scene including; spectral signature analysis (SSA) of the main recorded rock units; false-color composite (FCC); band-ratio (BR); principle component analysis (PCA), minimum noise fraction (MNF) and independent component analysis (ICA). Fusion images of 28.5m resolution bands with the 14.25m panchromatic band to enhance spatial resolution through imagery enhancement techniques. Maximum likelihood distance supervised classification technique (ML).
- c) Four RTC scenes (which were acquired in 2010) have been utilized in the present work named ALPSRP247800500, ALPSRP247800510, ALPSRP245320500, and ALPSRP245320510. These scenes were downloaded from the website <https://asf.alaska.edu>. Alaska Satellite Facility creates radiometrically terrain corrected (RTC) from PALSAR (Phased Array type L-band Synthetic Aperture Radar) images; a digital elevation model with spatial resolution 12.5m corrected and presented in the GeoTIFF format. These scenes were processed, mosaiced, and cropped to construct a hill-shade map with a spatial resolution of 12.5m for the study area, also utilized in the construction of a 3D prospect map for the selected areas.

The processing and analysis of the OLI data (Landsat-8) workflow (Figure 3 (a)) comprises the atmospheric correction and imagery enhancement techniques. This workflow was developed utilizing packages of software including ERDAS IMAGINE, ENVI-5.1, ArcGIS-10.1, and Google Earth Pro; to develop different images, hill-shade maps, and 3D perspective views. It is worth

mentioning that every single pixel of the constructed maps has been spectrally reviewed and verified by fieldwork.

4. Results

4.1. Spectral signature analysis (SSA)

Spectral signature analysis is a profile representing the reflectance and thermal signature of one pixel throughout several bands. The spectral signature of any rock depends on the spectral characteristics of its chemical constituents as well as its internal molecular structure. The spectral reflectance profiles were developed from the Landsat-8 OLI data (seven VNIR and SWIR bands) for the 19 rock units whose ages are ranging from the Precambrian to the Quaternary (Figure 3 (b)). The spectral profile of these rock units obeys a general decrease of the spectral reflectance (digital number) from band 7 to band 1. Each of these 20 rock units has a remarkable digital number (spectral reflectance) with bands 3, 4, 5, 6, and 7; whilst similar spectral reflectance has been recorded with bands 1, 2, and 8.

4.2. False-color composite images (FCC)

The OLI true-color image, 432 RGB (Red-Green-Blue) is shown in Figure 4 (a). Several false color composite images for RGB were constructed such as 753, 672, 652, 761, and 642 (based on the difference in spectral reflectance for each different rock unit). These false-color composite images (extracted from OLI data of Landsat-8) are valuable for the differentiation of the rock units and their applications in geological mapping.

The true-color composite 432 RGB (Figure 4 (a)) is a useful tool in the identification of the Thebes and Abu-Dabbab formations. The Thebes Formation is characterized by its whitish color with a scratched appearance and the Abu-Dabbab Formation is marked by its milky whiterough appearance with a brain-like weathering geometry.

False-color composite 642 and 672 RGB (Figures 4 (b) and 4 (c)) are effective in the discrimination of the Precambrian rock units (Metavolcanics, Metasediments, Dokhan volcanics, Hammamat sediments, younger granites and Post-Hammamat felsite) and the Miocene rock units.

False-color composites 671 and 652 RGB (Figures 4 (d) and 4 (e)) are effective in recognition of the Precambrian rock units in

addition to the Nubian sandstone and the Miocene rock units including the Ranga, Um Mahara and Abu-Dabbab formations.

The most operative false-color composite combination in the discrimination of different rock units is **753 RGB** (Figures 4 (f) and 5). It is used

to discriminate the Precambrian rock units (Metavolcanics, Metasediments, Dokhan volcanics, Hammamat sediments, younger granites, and Post-Hammamat felsite), the Nubian Sandstone, and the Miocene rock units in addition to the Oligocene basalt.

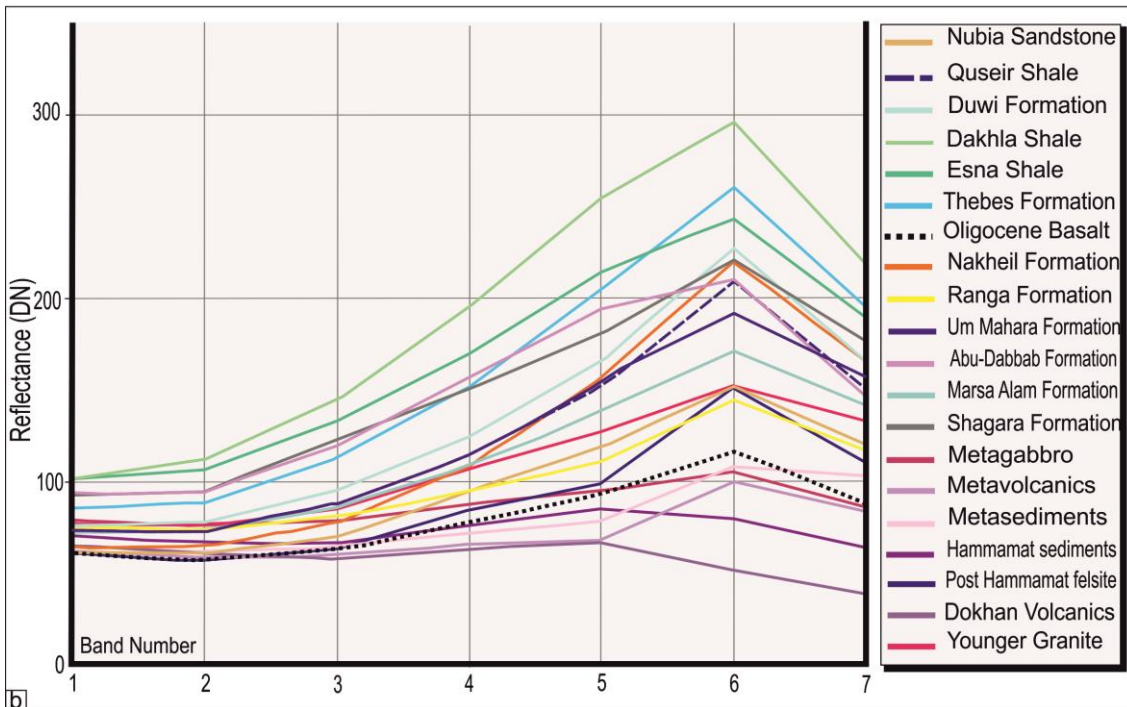
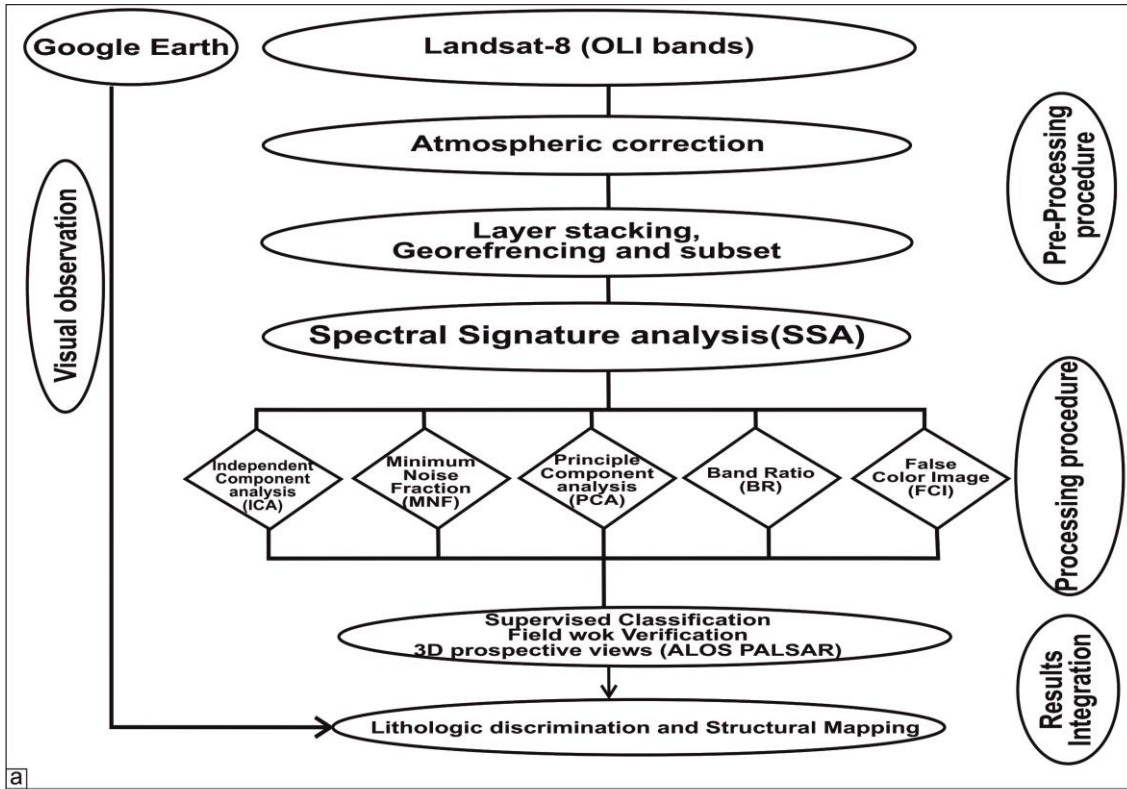


Figure 3. a. Flowchart showing the applied processing and analysis techniques in the present study; b. Spectral signature analysis of the mapped rock units.

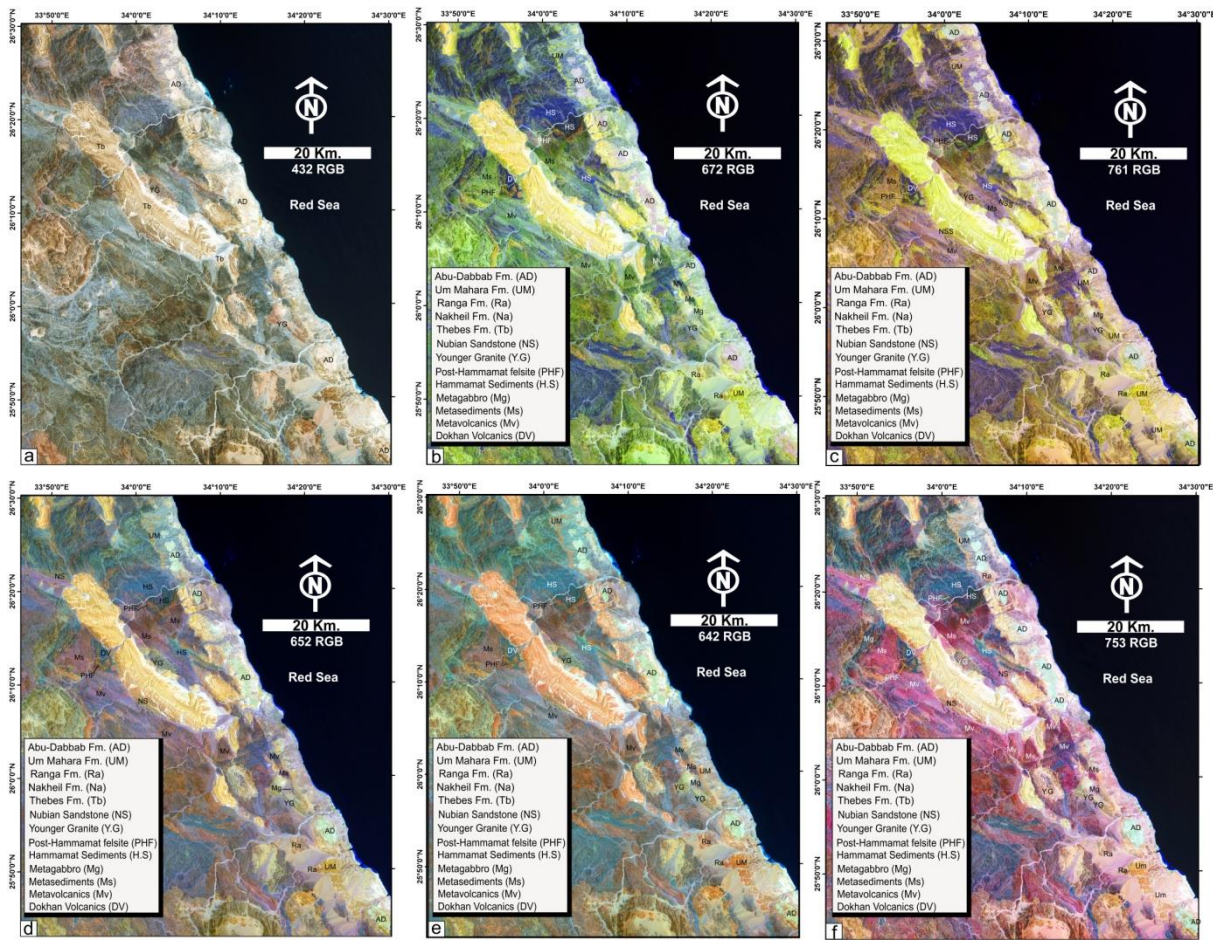


Figure 4. False color composite images (FCC) a. true colour image 432 RGB; b. False Color Composite 672 RGB; c. False Color Composite 671 RGB; d.False Color Composite 652 RGB; e. False Color Composite 642 RGB; f. False Color Composite 753 RGB.

4.3. Band-ratio images (BR)

Bandratio is the proportion of band to another band. It is a remote sensing technique utilized to differentiate between different rock units established on the rearrangement of different absorption bands. Band-ratio images are extracted through the division of the digital number value of one spectral band for each pixel by the value of the digital number of another one, and the resultant outcomes are plotted as an image [49-51]. SSA of the studied rock units shows absorption features at the bands 1, 2, and 3 and higher spectral reflectance at the bands 4, 5, 6, and 7. Based on the spectral signature analysis, several band ratios were developed as 2/1, 3/2, 3/4, 5/3, 5/4, 6/2, 6/4, 6/5, 6/7, and 7/4. Several composite Images (Figure (6)) had been constructed from these band ratios to define different rock units.

(2/1, 5/3, 7/4) RGB (Figure 6 (a)) is effective in recognition of the Precambrian rock units, the Pre-rift Nubian sandstone and the Syn-rift rock units including the Ranga, Um Mahara, and Abu-Dabbab formations.

(3/2, 7/4, 5/4) RGB (Figure 6 (b)) is efficient in the differentiation of the Precambrian rock units, the Nubian sandstone and Duwi formations and the syn-rift rock units including the Oligocene basalt, Ranga, Um Mahara, and Abu-Dabbab formations.

(6/4, 3/2, 2/1), (2/1, 6/4, 3/4), (6/2, 6/5, 6/7) and (7/4, 5/3, 2/1) RGB (Figures 6 (c-f)) are powerful images in discrimination of the Precambrian rock units, the Pre-rift Nubian Sandstone and Duwi formations and the syn-rift (Miocene and Pliocene) rock units in addition to the Oligocene basalt.

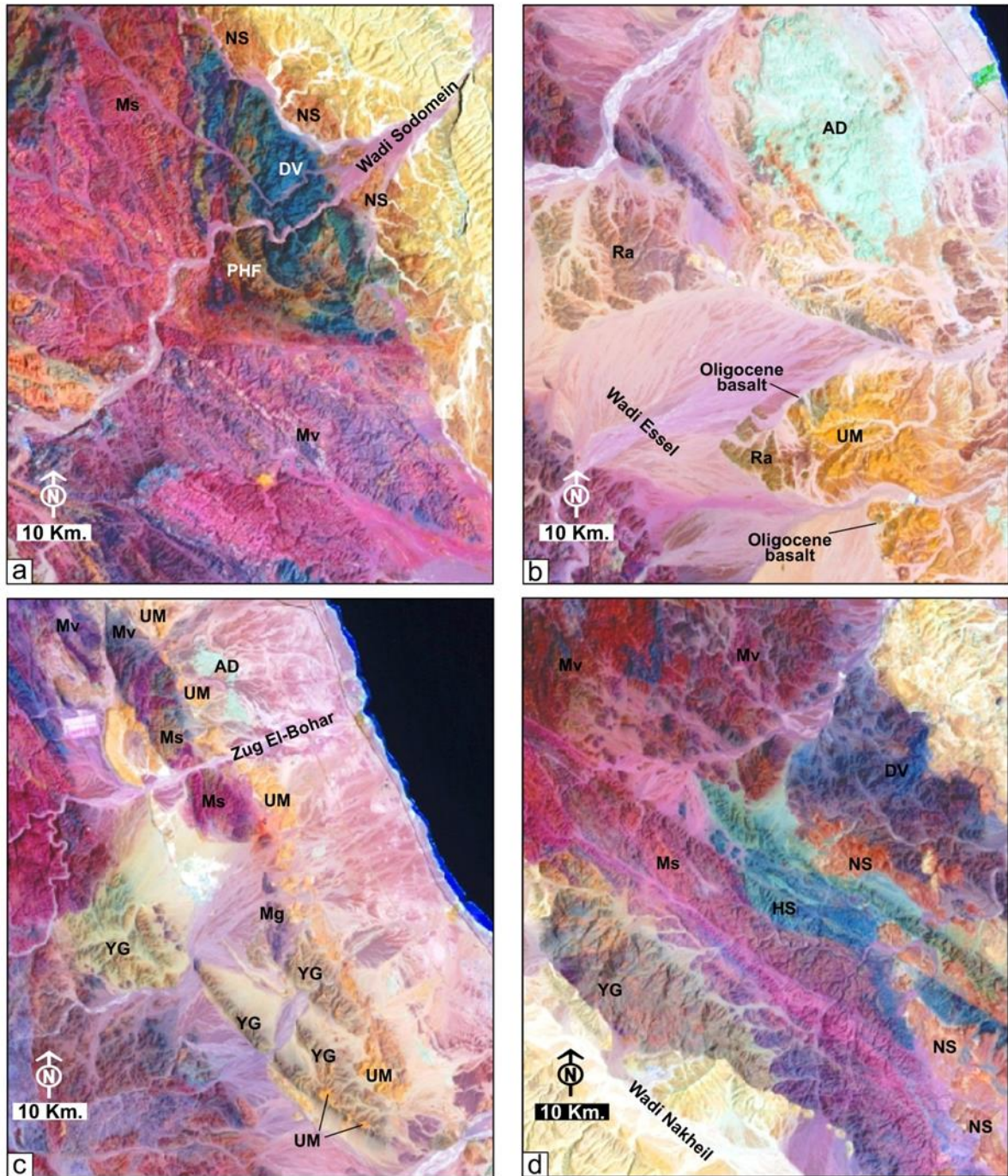


Figure 5. False color composite 753 RGB a. Wadi Sodomein; b. Syn-rift rock units at Wadi Essel; c. Zug El-Bohar; d. Wadi Nakheil.

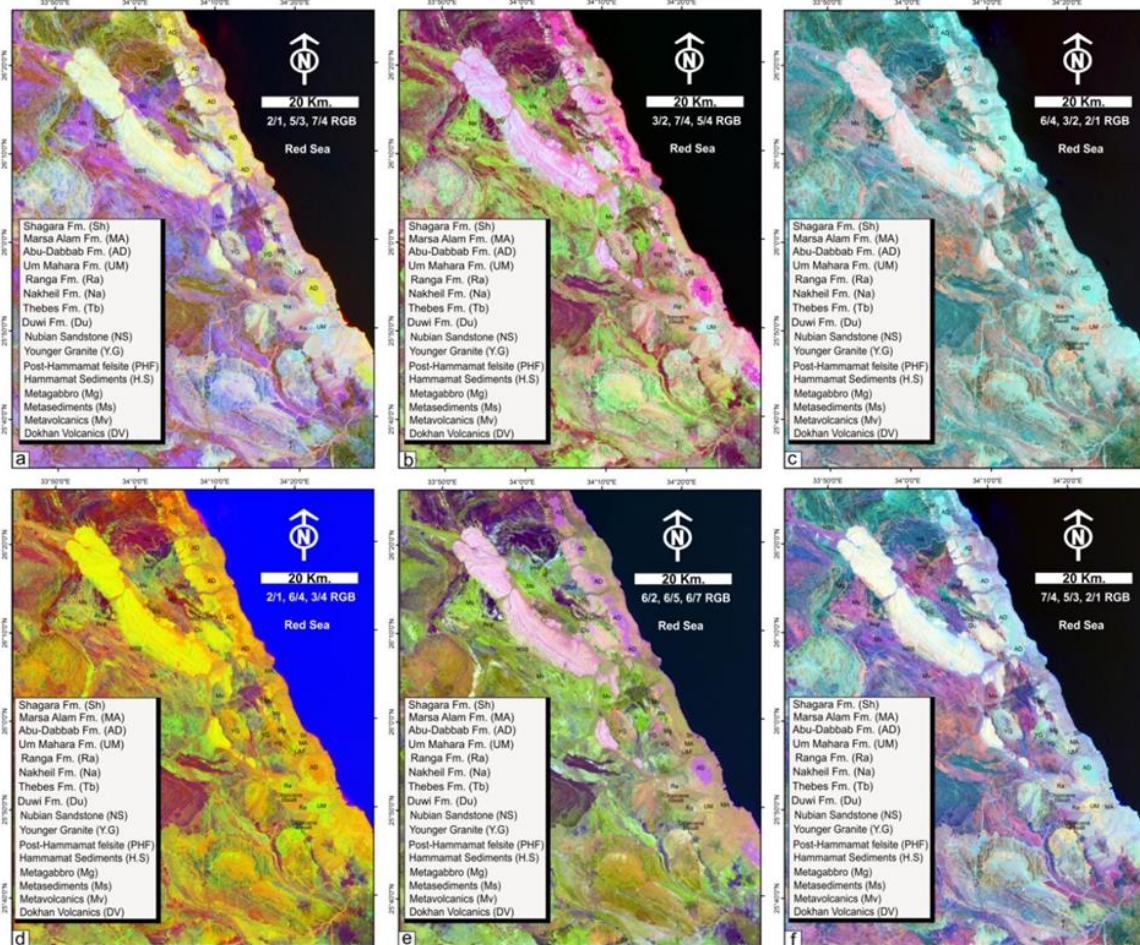


Figure 6. Band ratio images (BR) a. (2/1, 5/3, 7/4) RGB; b. (3/2, 7/4, 5/4) RGB; c. (6/4, 3/2, 2/1) RGB; d. (2/1, 6/4, 3/4) RGB; e. (6/2, 6/5, 6/7) RGB; and f. (7/4, 5/3, 2/1) RGB.

4.4. Principle component analysis (PCA)

The principal component analysis is a remote sensing procedure that changes over a set of conceivably correlated variable observations into a set of linearly uncorrelated values [52]. It is utilized to constrict the data essence of a number of the spectral bands or dimensionality-reduction from the number of spectral bands in two or three principle components [53]. The processing of the crude data utilizing PCA produces new imagery that is more expandable than initial ones [53]. The principal component analysis is utilized for the detection of different rock units from Landsat-8

data. Seven principle component bands were deduced from the OLI data (visible-NIR and SWIR bands). Analysis of the principle components of eigenvector loading gave an obvious conception regarding the selection of the bands (Figures 7 (h) and 7 (i), Table 2), which enhance the color differences between the rock units. The first PCA band (PC1) contains about 98.6% of the data and the rest bands (PC2-7) appear noisy (due to little variance of the data); however, these bands retain their capability for lithological investigation.

Table2. Eigenvector values of principal component analysis (PCA) of the seven OLI Landsat-8 bands of the studied area.

PC	Band No.1	Band No.2	Band No.3	Band No.4	Band No.5	Band No.6	Band No.7	Eigen values %
PC1	0.068276	0.1127	0.231123	0.345846	0.453827	0.601355	0.491958	98.6
PC2	-0.20491	-0.255261	-0.360195	-0.439457	-0.429604	0.393945	0.479832	0.9
PC3	-0.097039	-0.198338	-0.332217	-0.172436	0.376715	0.512427	-0.637689	0.287942
PC4	0.442211	0.434556	0.306363	-0.140345	-0.49473	0.427734	-0.272655	0.146478
PC5	0.576134	0.301263	-0.379864	-0.446712	0.389091	-0.188841	0.215427	0.04796
PC6	-0.350209	0.073997	0.604954	-0.657637	0.267036	-0.043078	0.01608	0.006972
PC7	0.542039	-0.773129	0.319921	-0.076152	0.010453	-0.011155	0.009114	0.001389

The visual investigations of the grayscale seven PCA bands (Figures 7 (a-g)) showed the followings: PC1 distinguishes the Precambrian basement rocks from the sedimentary rock. PC2 defines the Metavolcanics, Hammamat sediments and Post-Hammamat felsite of the Precambrian rocks in addition to the Pre-rift deposits (brighter light grey colour), PC3 discriminates the Precambrian Younger Granite, Hammamat sediments and Post-Hammamat felsite as well as the Duwi Formation and Esna Shale in addition to the Syn-rift Miocene deposits. PC4 defines the Post-Hammamat felsite, Pre-rift deposits and Oligocene Basalt. PC5 discriminates between the Duwi Formation, Nakheil Formation and Um Mahara Formation. PC6 highlights the Post-Hammamat felsite, the Duwi Formation and the Abu-Dabbab Formation. PC7 distinguishes the Precambrian rocks from the sedimentary rocks. Several RGB PC composite images (Figure 8) were developed to define different rock units as follows:

(PC2, PC1, PC3) and (PC2, PC5, PC6) RGB (Figure 8 (a)) composites are utilized in the discrimination of the Precambrian rock units (Metavolcanics, Metasediments, Dokhan volcanics, Hammamat sediments, younger granites, and Post-Hammamat felsite), the Nubian Sandstone and the Duwi Formation as well as the syn-rift deposits (Oligocene to Pliocene) as well as the Oligocene basaltic flows.

(PC6, PC4, PC2), (PC4, PC5, PC2) RGB (Figures 8 (b-d)) composite highlight the outline of the Precambrian rock units (Metavolcanics, Metasediments, Dokhan volcanics, Hammamat sediments, younger granites, and Post-Hammamat felsite), Pre-rift the Nubian Sandstone, Duwi Formation and Esna Shale, and the Syn-rift (Oligocene-Pliocene) rock units in addition to the Oligocene basalt and recent coral reefs.

4.5. Minimum noise fraction (MNF)

The minimum noise fraction (MNF) is a remote sensing image enhancement technique that has been used to diminish the computational requirements through the isolation of the noise from the signal in the data set. MNF was carried out on seven bands (VNIR-VRE-SWIR bands) of the OLI data (Landsat-8). Analysis of the MNF eigenvector gave a clear idea about the selection of the bands, which enhance the color differences between the rock types. Based on statistical studies, several MNF composite images (Figure 9) were generated to determine the different rock units as follows.

MNF 523 RGB (Figure 9 (a)) composite image define the boundaries of some Precambrian Basement rocks units (Metavolcanics, Metasediments, Dokhan volcanics, Hammamat sediments, younger granites, and Post-Hammamat felsite), the Nubian Sandstone as well as the Miocene rock units.

MNF 645 RGB (Figure 9 (b)) composite could be utilized in the identification of the Precambrian rock units, the Pre-rift Duwi Formation and Esna Shale in addition to the Syn-rift rock units.

MNF 546 RGB (Figure 9 (c)) composite is an effective tool in the differentiation of the basement rock units, the Pre-rift (Nubian sandstone, Duwi Formation and Esna Shale) and the Syn-rift rock units (the Nakheil, Oligocene Basalt, Ranga, Um Mahara, Abu-Dabbab formations). The Quaternary deposits are characterized by dark blue to violet color.

MNF 546 RGB (Figure 9 (d)) composite is similar to the aforementioned composed image but it is more powerful in the definition of the Marsa Alam and Shagra formations, in addition to recent Red Sea corals.

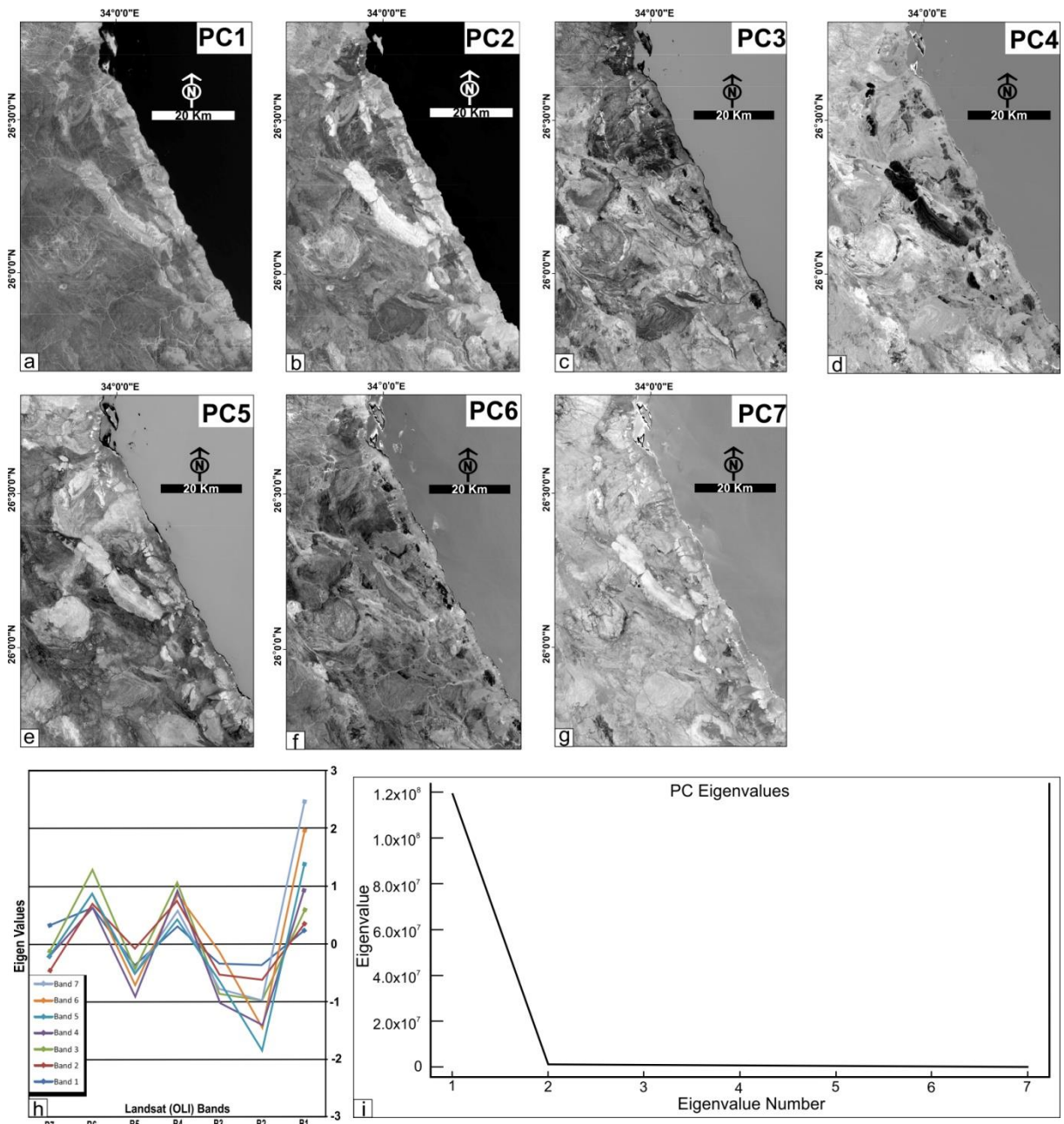


Figure 7. a-g. Seven principle components generated from Landsat 8 (OLI) Visible, NIR, and SWIR bands of the studied area, h and i. Eigen values of the (OLI) Visible, NIR, and SWIR bands.

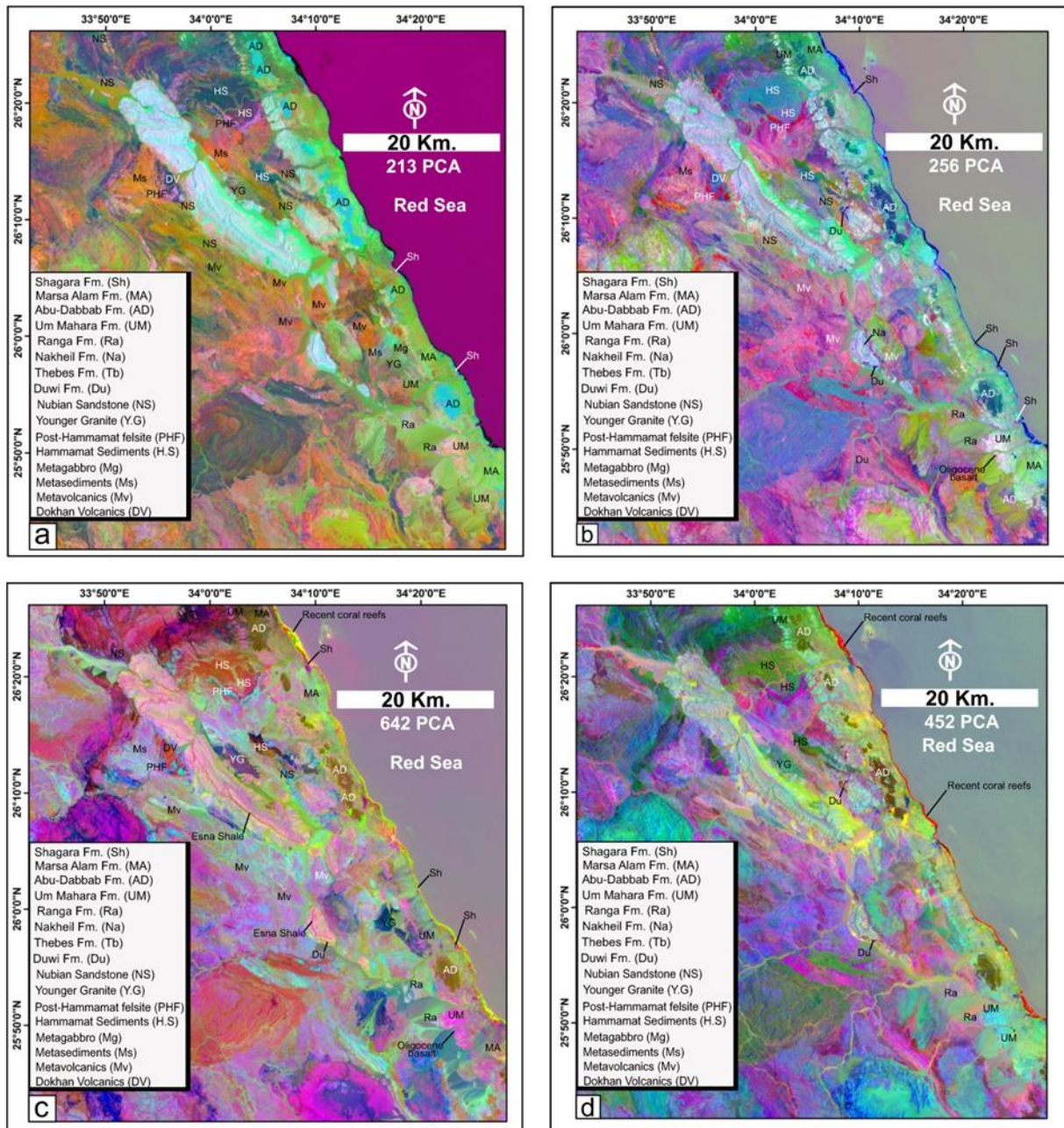


Figure 8. Principle Component Analysis (PCA);a. (PC4, PC3, PC2) RGB; b. (PC2, PC5, PC7) RGB; c. (PC4, PC5, PC2) RGB; and d.(PC7, PC5, PC2) RGB.

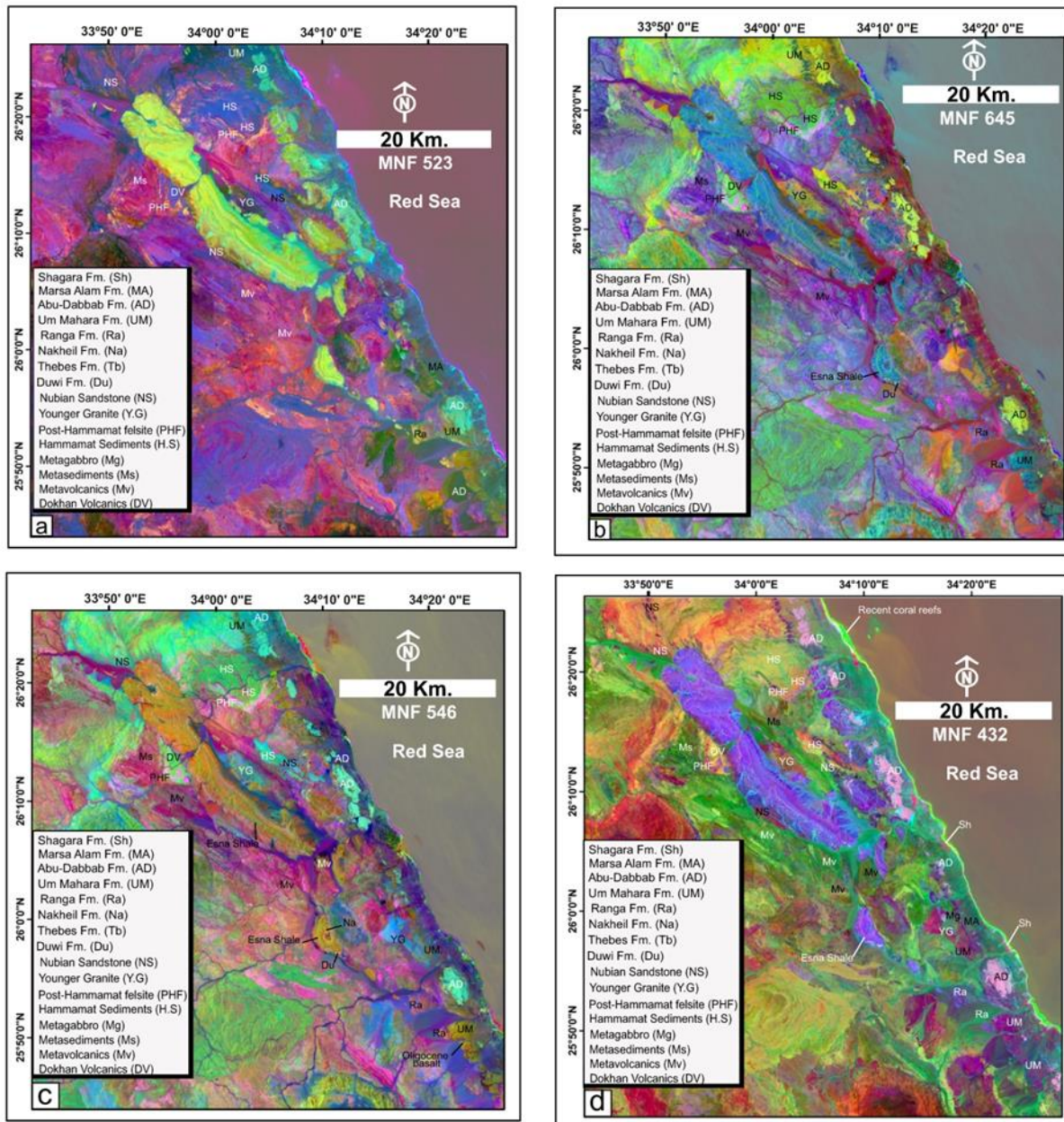


Figure 9. Minimum noise fraction (MNF); a. (5, 2, 3) RGB; b. (6, 4, 5) RGB; c. (5, 4, 6) RGB; and d.(4, 3, 2) RGB.

4.6. Independent component analysis (ICA)

ICA is a statistical methodology utilized for the subdivision of complex datasets into separate components (sub-parts). It originates from a blind source and seeks the transformation of the observed multidimensional vector into many components distinct from one another statistically (as much as possible). The ICA is a powerful tool in the differentiation of features, however, they settle on a small portion of a pixel in the image [45-55]. ICA has performed on the Landsat-8 OLI seven bands. The eigenvector analysis provides information about band selection, enhancing the identification of various rock units. According to

this statistical analysis, several ICA transformation composite images (Figure 10) have been constructed as follows:

ICA transformation 354 RGB image (Figure 10 (a)) is effective in the differentiation of the Dokhan volcanics, Younger granite, Post-Hammamat felsit, some alteration in the Metavolcanics in addition to Oligocene basalt.

ICA transformation 452 RGB image (Figure 10 (b)) is a useful tool in discrimination of the Dokhan volcanics, Younger granite, Post-Hammamat felsit, some alteration in the Metavolcanics, Nubian Sandstone, Duwi

Formation, Oligocene Basalt, Ranga Formation, Um Mahara, Abu-Dabbab, MarsaAlam Formation, and the patch reefs of the Shagra Formation.

ICA transformation 354 RGB image (Figure 10 (c)) is efficient in the differentiation of the interlocking Metavolcanics and Younger granite at the entrance of Wadi Nakheil in addition to the Precambrian rock units (Hammamat sediments, Younger granite, Post-Hammamat felsite), the

syn-rift rock units including the Oligocene basalt, Ranga, Um Mahara, Abu-Dabbab, MarsaAlam, and Shagra formations.

ICA transformation 354 RGB image (Figure 10 (d)) is vital in the identification of the syn-rift rock units including the Nakheil Formation at the core of Gebel Duwi Syncline, Ranga, Um Mahara, and Abu-Dabbab, MarsaAlam, and Shagra formations in addition to the recent coral reefs.

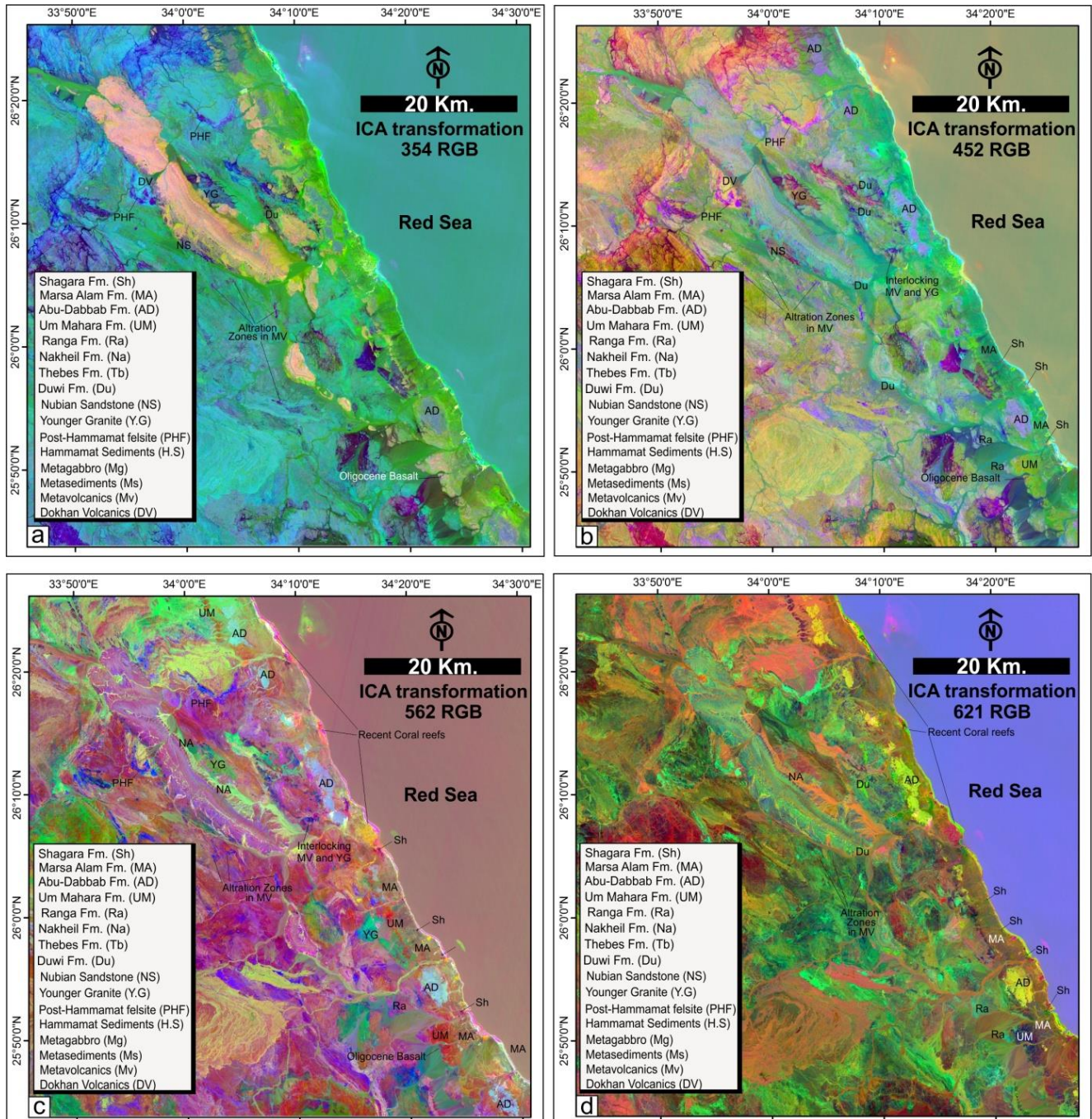


Figure 10. Independent Component Analysis (ICA) transformation; a. (3, 5, 4) RGB; b. (4, 5, 2) RGB; c. (5, 6, 2) RGB; and d.(6, 2, 1) RGB.

4.7. Maximum likelihood distance supervised classification (ML)

After defining different sample areas (training areas) based on their spectral characteristics, the maximum likelihood classifier pays attention to the centre, shape, size, and orientation of the clusters. This is performed through the calculation of statistical distance (depending on the covariance matrix and mean values of the clusters, [56]). ML-supervised classification gave high

accuracy results, where it differentiates 25 classes, into 25 colors corresponding to certain rock units (Figure 11). A new detailed geologic map has been constructed based on ML supervised classification aided with field verification. It is worth mentioning that three different types of the Younger Granite, two types of Metavolcanics, two types of Metasediments, and two different types of Hammamat sediments could be differentiated based on this classification analysis.

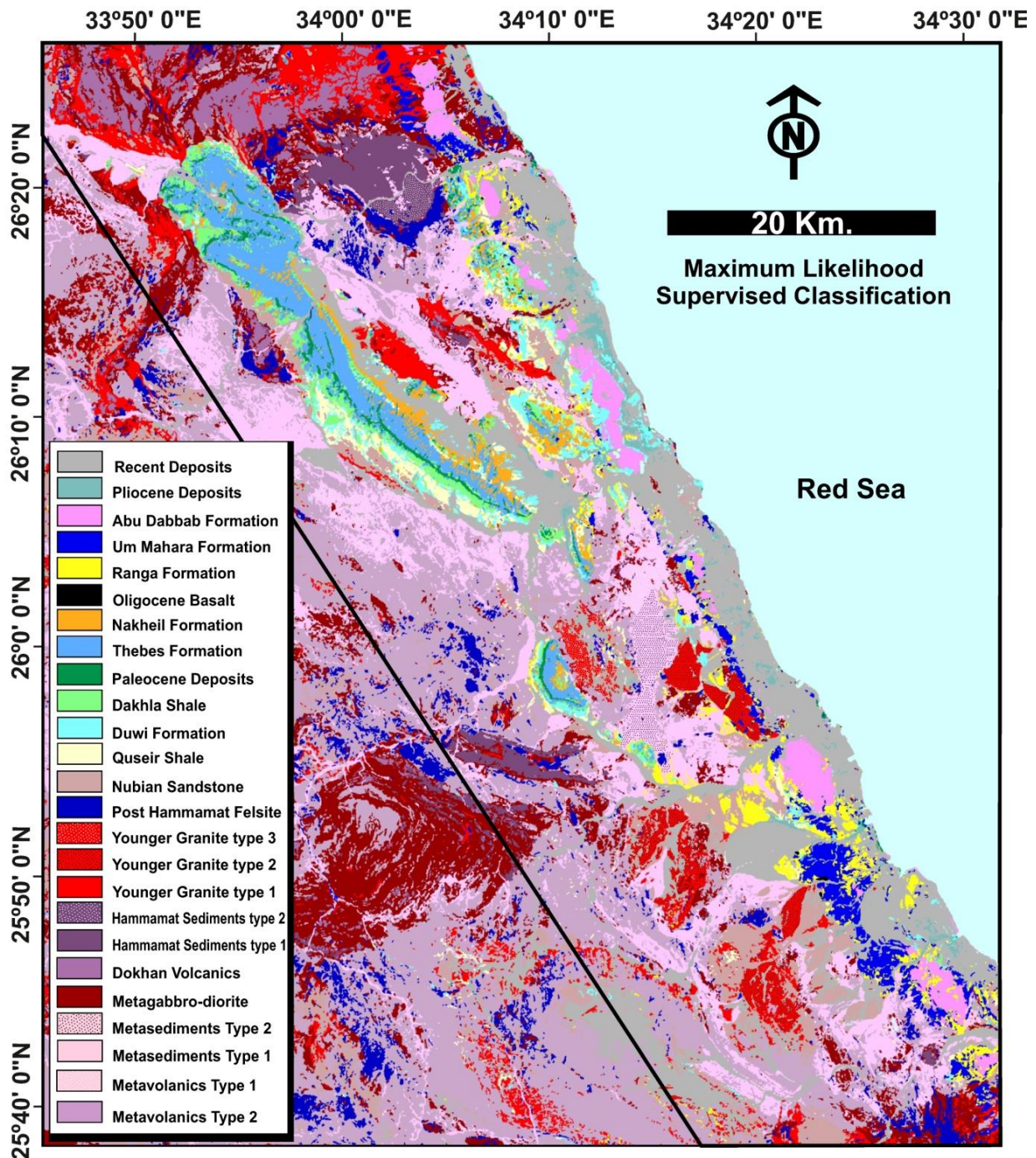


Figure 11. Maximum likelihood supervised classification of the studied area.

4.8. Digital elevation model (DEM)

The following work utilizes radiometrically terrain-corrected (RTC) DEM data extracted from the PALSAR with a spatial resolution of 12.5m. Hill-shade map was constructed for the studied area to discriminate between different geomorphologic highlands and lowlands. Several geomorphologic highlands (as G. Um Zarabit, G. Duwi, G. Hamadat, G. Anz, G. Atshan, and G. Hidusi) were recognized through these hill-shade maps (Figure 12 (a)) from geomorphologic lowlands (as W. Queih, W. Saqi, W. Sodomim, W. Nakheil, W. Ambagi, Wadi Hamadat, W. Essel, W. Sharm El-Bahari, W. Sharm El-Qebli, W. Beda El-Atshan, W. Zug El-Bohar, and W. Iseiwid). A structural architecture map (Figure 12 (a)) could be constructed based on this hill-shade map. Two 3D perspective view images have been generated to validate these structural elements (Figures 12 (b) and 12 (c)) based on DEM data (12.5m spatial resolution), which merged with information derived from the OLI data (Landsat-8). Integration between results of the different remote sensing techniques, DEM and detailed fieldwork; a new structural map (Figure 13) displays more enhancement than previously published ones [57-60] has been constructed. The

studied area structural framework is predominated by NW-striking hard-linked rift-related normal dip-slip faults (Figure 14 (a)) with some E-W to ENE-striking normal dip-slip normal faults (cross elements). Kilo-meter scale fault propagating folds (Figure 14 (b)) are developed at the hanging wall of these hard linked faults (e.g. Gebel Anz double plunging syncline (Figure 14 (c)), Gebel Duwi double plunging syncline (Figure 14 (d)), Gebel Atshan Plunged syncline (Figure 14 (e)), Gebel Hamadat double plunged Synclines (Figure 14 (f)), Gebel Rewagen plunged syncline (Figure 2 (i)), Zug El-Bohar double plunged syncline). The northern margin of the Gebel Duwi syncline could be described as an overlapping convergent transfer zone [61] between NW-striking fault segments, namely as Duwi Accomodation Zone [59]. This Accomodation zone is developed between the SW-dipping hard-linked fault (Nakheil Fault segment of [59]) and the NE-dipping hard-linked fault (Kallahin Fault segment of [59]). Breached relay ramps are developed through the NNW, WNW and NW-striking linked fault segments. Two of these breached relay ramps are developed at the northern and southern parts of the Gebel Hamrawin and one at Gebel Nakheil (Figure 14 (g)) [60].

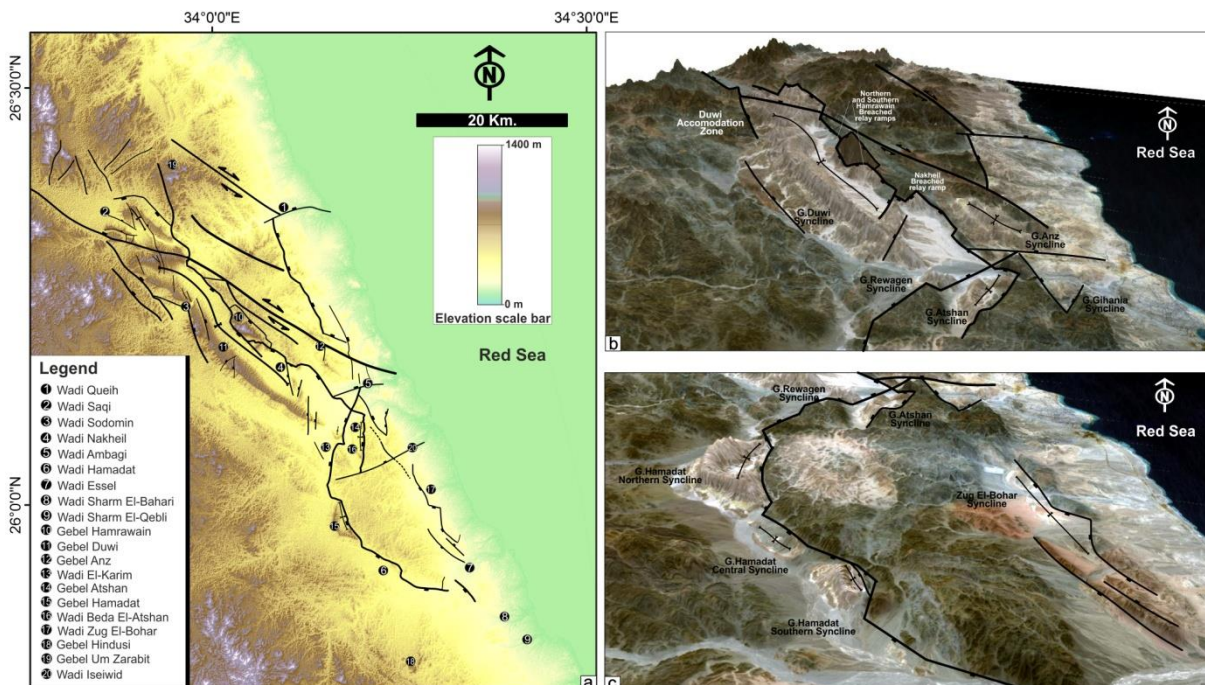


Figure 12. a. Structural architecture map based on hill-Shade view; b. 3D perspective view shows the structural architecture of the northern part of the studied area; and c. 3D perspective view shows the structural architecture of the southern part of the studied area.

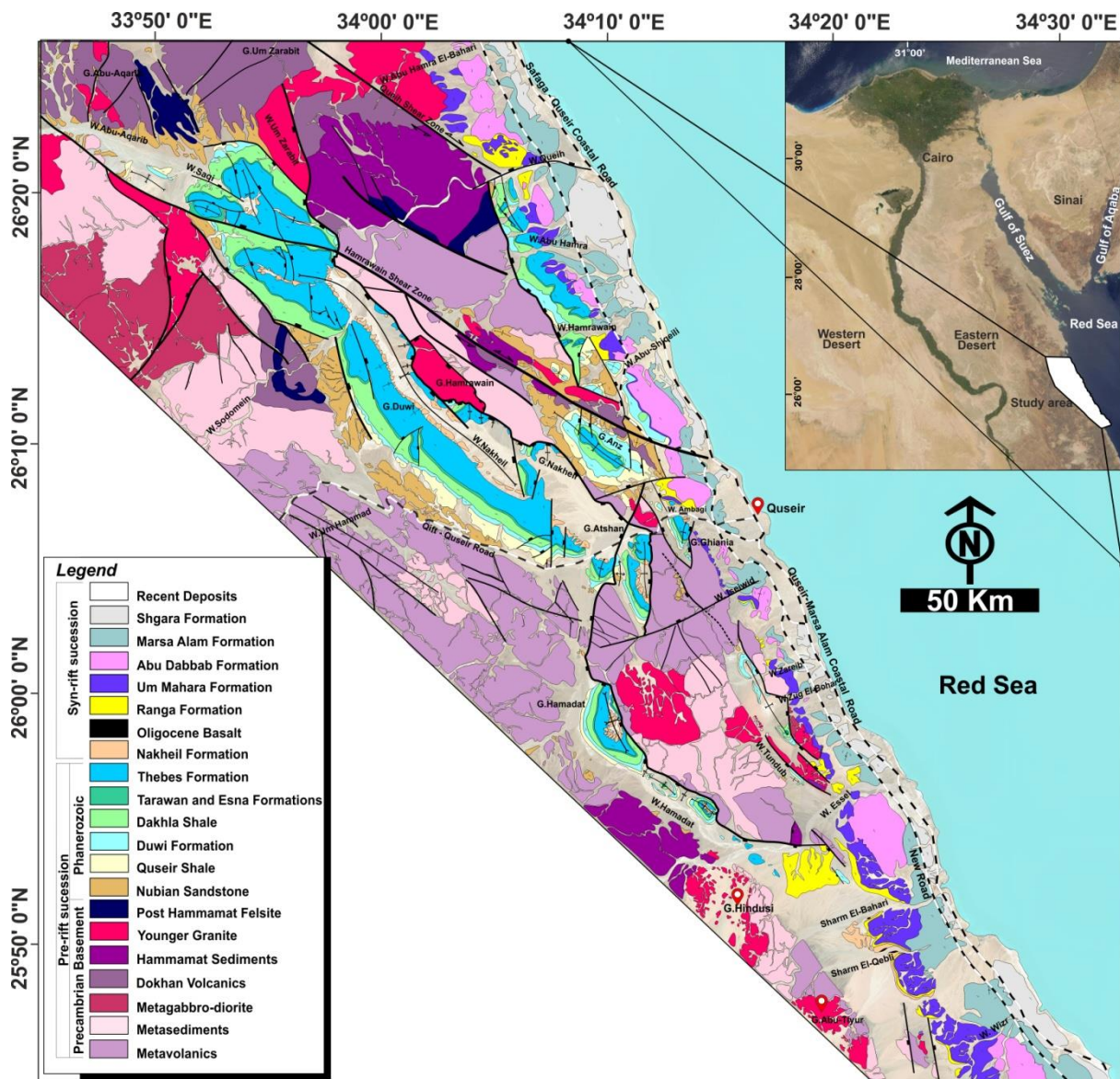


Figure 13. Detailed structural map of the studied area (Modified after Conoco, 1987 and Khalil and McClay, 2001, 2002 and 2018).

The structural framework of the studied area is dominated by NW to NNW-striking faults with sub-ordinate ENE-strike. Several hydrothermal alteration zones form at the intersection of these faults and the Metavolcanics (sites of upward fluid flux), which are traced in the studied area using various remote sensing techniques. They are considered good sites for mineral and ores (e.g. lead and zinc; see Figure 2b; copper, tungsten, and beryllium) exploration [62]. Lead and zinc mineralization occurs in the Um Gheig area (to the south of the study area, along the Red Sea coastal plain). This mineralization is developed at

the intersection of the Syn-rift deposits (Um-Mahara Formation) with the NW-striking rift-related fault system [63]. At the Missikat area (to the north of the study area), uranium and sulphide (chalcopyrite, pyrite, sphalerite, galena, and molybdenite) mineralization are developed along the intersection of the ENE-striking faults with the Younger Granites [64]. Based on the aforementioned observations, there is a complete match with the new exploration concept introduced by [65], which considers mineral investigation in terms of spatial and genetic factors instead of structural criterion.

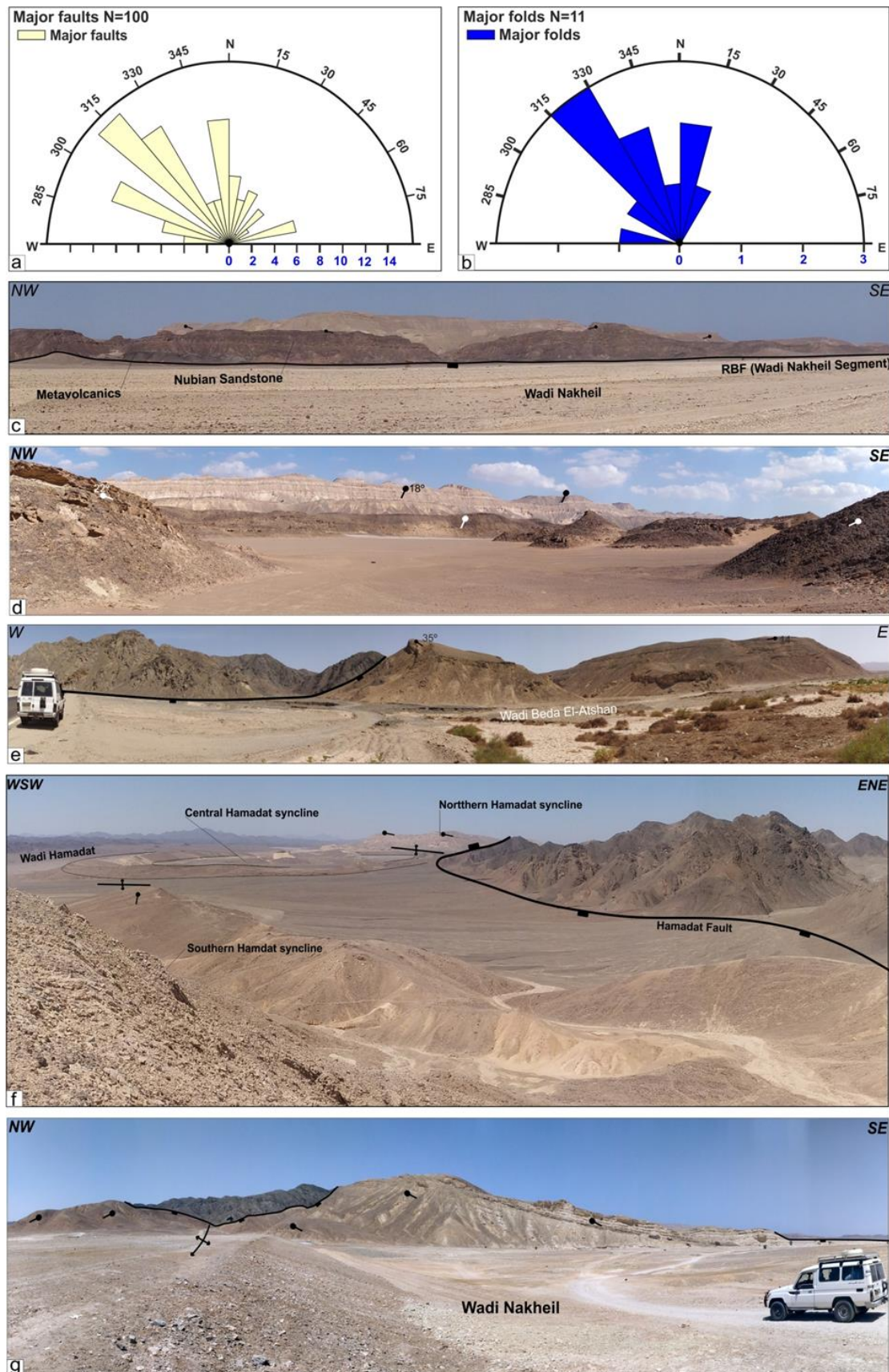


Figure 14. a&b. Rose diagram showing the main trend of the major faults, and folds in the area; c. Field Photograph showing Gebel Anz double plunged syncline; d. Field Photograph showing the NE-dipping limb of the Gebel Duwi double plunged syncline; e. Field Photograph showing the Gebel Atshan syncline; f. Field Photograph showing Gebel Hamadat fault and its associated syncline (Northern, Central and Southern) folds; g. Field Photograph showing breached relay ramp between two NW-striking fault segments at Gebel Nakheil.

5. Conclusions

The present work introduced a new high-resolution enhanced structural map of the studied area through integration between visual observation of Google Earth satellite images, various image enhancement techniques of the OLI (Landsat-8 image), and radiometrically terrain corrected (RTC) extracted from the PALSAR images aided with fieldwork. Various digital enhancements of the OLI data (Landsat-8) were carried out by implementing the SSA, FCC, BR, PCA, MNF, and ICA to characterize the different rock units of the studied area. **Several band combinations were constructed as RGB images such as 753, 672, 652, 761, and others** (based on the difference in spectral reflectance for each different rock unit). The most operative false-color composite combination is **753 RGB** used to discriminate the Precambrian rock units (Metavolcanics, Metasediments, Dokhan volcanics, Hammamat sediments, younger granites, and Post-Hammamat felsite), the Nubian Sandstone, and the Miocene rock units in addition to the Oligocene basalt. Based on the spectral signature analysis several **band ratio images** such as (2/1, 5/3, 7/4), (3/2, 7/4, 5/4), (6/4, 3/2, 2/1), (2/1, 6/4, 3/4), (6/2, 6/5, 6/7) and (7/4, 5/3, 2/1) RGB were developed. **These band ratio composite** images are a powerful tool in discrimination of the Precambrian rock units, the Pre-rift Nubian Sandstone and Duwi formations and the syn-rift (Miocene and Pliocene) rock units in addition to the Oligocene basalt. **PCA composite** images as (PC4, PC3, PC2), (PC2, PC5, PC7), (PC4, PC5, PC2), and (PC7, PC5, PC2) RGB were constructed based on analysis of PCs eigenvector. These PCA composite images highlight the Precambrian rock units (Metavolcanics, Metasediments, Dokhan volcanics, Hammamat sediments, younger granites, and Post-Hammamat felsite), Pre-rift the Nubian Sandstone, Duwi Formation and Esna Shale, and the Syn-rift (Oligocene - Pliocene) rock units in addition to the Oligocene basalt and recent coral reefs. **MNF composite** images such as MNF 523, MNF 645, MNF 546 and MNF 432, RGB are an effective tool in the differentiation of the basement rock units, the Pre-rift (Nubian sandstone, Duwi Formation and Esna Shale), and the Syn-rift rock units (the Nakheil, Oligocene Basalt, Ranga, Um Mahara, Abu-Dabbab formations) in addition to the Quaternary deposits. **ICA transformation composite** images as (5, 2, 3), (6, 4, 5), (5, 4, 6) and (5, 4, 6) RGB were

constructed based on ICAs eigenvector analysis. These images were efficient in the differentiation of features with small pixel spaces, e.g. the interlocking Metavolcanics and Younger granite at the entrance of Wadi Nakheil, Oligocene basalt and the patchy appearance of the Shagara Formation. It is worth mentioning that three different types of the Younger Granite, two types of Metavolcanics, two types of Metasediments, and two different types of Hammamat sediments could be differentiated based on this classification analysis, based on ML supervised classification aided with field verification. DEM images with a spatial resolution of 12.5m (RTC data extracted from PALSAR) was utilized to delineate the structural architecture of the studied area through a hill-shade map and 3D perspective view images. Integration between different remote sensing techniques and DEM aided with the detailed fieldwork help to construct a new structural map with more enhancement than previously published ones [57-60]. From the structural point of view, the studied area was dominated by NW to NNW-striking faults; several hydrothermal alteration zones were developed in the Metavolcanics along these faults and traced through the application of different remote sensing techniques (especially the ICA and MNF). These fault-related alteration zones were considered prospect sites for minerals and ores (e.g. lead and zinc, copper, tungsten, and beryllium) exploration [62]. The remote sensing technique is a powerful tool not only in lithological and structural mapping but also it is very informative in the field of mineral exploration through matching the geochemical characteristics of each mineral with its spectral signature obtained from remote sensing data [9 and 62]. At several locations, intersections between faults and different rocks were considered good sites for mineral investigation, which matched the new exploration concept introduced by [65] considering mineral investigation in terms of spatial and genetic factors instead of structural criterion.

References

- [1]. Rowan, L.C., Mars, J.C., and Simpson, C.J. (2005). Lithologic mapping of the Mordor NT, Australia ultramafic complex by using the Advanced Spaceborne Thermal Emission and Reflection Radiometer (ASTER). *Remote Sens. Environ.*, 99 (1-2), 105-126.
- [2]. Hassan, S., Abdeen, M.M., El-Kazzaz, Y.A., and Attia, G.M. (2008). Characterization of Oligocene sands and gravels, Wadi Ghoweiba, Northwest Gulf of Suez, Egypt, using spectral- signature and principal

component analysis of Terra Aster images. The Egyptian Journal of Remote Sensing and Space Sciences, 11:73-92.

[3]. Afify, A.A., Arafat, S.S., AboelGhar, M., and Khader, M.H. (2010). Physiographic soil map delineation for the Nile alluvium and Desert outskirts in middle Egypt using remote sensing data of EgyptSat-1. Egypt J Remote Sens Space Sci 13 (2):129-135.

[4]. Amer, R., Kusky, T., and Ghulam, A. (2010). Lithological mapping in the Central Eastern Desert of Egypt using ASTER data. J Afr Earth Sc 56 (23):75-82

[5]. Arnous, M. and Sultan, Y. (2014). Geospatial technology and structural analysis for geological mapping and tectonic evolution of Feiran-Solaf metamorphic complex, South Sinai, Egypt. Arab J. Geosci., 7, 3023-3049.

[6]. Hassan, S.M. and Sadek, M.F. (2017). Geological mapping and spectral based classification of basement rocks using remote sensing data analysis: the Korbiai-Gerf nappe complex, South Eastern Desert, Egypt. J. African Earth Sci. 134, 404-418.

[7]. Badr, Y.S. (2017). Application of remote sensing technique in geologic mapping of hydrothermal alteration zones and possible radioactive potentialities at Ras Barud - Um Tagher area, North Eastern Desert, Egypt. PhD Thesis, Faculty of Science, Menoufiya University, Menoufiya, 164p.

[8]. Hamimi, Z., Hagag, W., Kamh, S., and El-Araby, A. (2020). Application of remote-sensing techniques in geological and structural mapping of Atalla Shear Zone and Environs, Central Eastern Desert, Egypt. Arab. J. Geosci. 2020, 13, 414.

[9]. Ghasemzadeh, S., Maghsoudi, A., Mahyar Yousefi, M., and Mark J. Mihalasky, M.J. (2022). Information value based geochemical anomaly modeling: a statistical index to generate enhanced geochemical signatures for mineral exploration targeting. Appl. Geochem. 136, 105177.

[10]. Saed, S., Aziz I., H., Daneshvar, N., Afzal, P., S.A. Whattam, S.A., and Mohammad, Y.O. (2022). Hydrothermal alteration mapping using ASTER data, Takab-Baneh area, NW Iran: A key for further exploration of polymetal deposits. Geocarto International, 1-27.

[11]. Mirsepahvand, F, Jafari, M. R., Afzal, P., and MA Arian, M.A. (2022). Identification of Alteration Zones using ASTER Data for Metallic Mineralization in Ahar region, NW Iran Journal of Mining and Environment 13 (1), 309-324.

[12]. El Gammal, E.M., Salem, S.M., and Greiling, R.O. (2013). Applications of geomorphology, tectonics, geology and geophysical interpretation of, East Kom Ombo depression, Egypt, using Landsat

images. Egypt J Remote Sens Space Sci 16 (2):171-187.

[13]. Sadeghi, B., Khalajmasoumi, M., Afzal, P., Parviz Moarefvand, P., Yasrebi, A. B., Andy Wetherelt, A., Foster, P., and Ziazarifi, A. (2013). Using ETM+ and ASTER sensors to identify iron occurrences in the Esfordi 1:100,000 mapping sheet of Central Iran. Journal of African Earth Sciences 85 (2013), 103-114.

[14]. Hamed, M. S. and Abdel Khalek, A. (2015). 3d Digital Geological Mapping and Lithological Characterization of The Northwestern Margin of The Gulf of Suez, Egypt By Integration of Remotely Sensing Data. Proceedings of the 15th International Multidisciplinary Scientific GeoConference SGEM 2015, Volume 1.

[15]. Pour, A.B. and Hashim, M. (2015). Hydrothermal alteration mapping from Landsat-8 data, Sar Cheshmeh copper mining district, south-eastern Islamic Republic of Iran. J. Taibah Univ. Sci. 9, 155-166.

[16]. Salem, S.M. and El Gammal, E.A. (2015). Iron ore prospecting East Aswan, Egypt using remote sensing techniques. Egypt J Remote Sens Space Sci 16 (2):195-206.

[17]. Seleim, A. M. and Hamed, M. S. (2016). Applications Of Remote Sensing In Lithological Mapping Of East Esh El Malaha Area, Southwest Gulf Of Suez–Egypt. International Journal of Scientific and Engineering Research, 7 (12): 691-701.

[18]. Khawfany, A., Aref, M.A., Matsah, M.I., and Taj, R.J. (2017). Utilizing Landsat-8 data in mapping of sabkha, mangroves, and land covers in Jizan coastal plain, southwestern Saudi Arabia. Arab. J. Geosci. 10 (5).

[19]. Hassan, S., El Kazzaz, Y., Taha, M., and Mohammad, A. (2017). Late Neoproterozoic basement rocks of Meatiq area, Central Eastern Desert, Egypt: petrography and remote sensing characterizations. J Afr Earth Sc 131:14-31.

[20]. Hammam, A., Gaber, A., Abdelwahed, M., and Hamed, M.S. (2018). Geological mapping of the Central Cairo-Suez District of Egypt, using space-borne optical and radar dataset, The Egyptian Journal of Remote Sensing and Space Sciences, 23 (3): 275-285.

[21]. Hamed, M. S., Shallaly, N. A., Abdel Ghani, I. M., Badr, Y. S., and Sayed, S. A. (2020). Application of Remotely Sensing Data in the Geologic and Radioactive Mapping of Wadi Fatirah Precambrian Rocks, North Eastern Desert, Egypt. Nuclear Sciences Scientific Journal 9: 227- 253.

[22]. Mohamed, T.A.M., Al-Naimi, L. S., Mgbejedo, T. I., and Agoha, C.C. (2021). Geological mapping and mineral prospectivity using remote sensing and GIS in parts of Hamissana, Northeast

Sudan. Journal of Petroleum Exploration and Production (2021) 11:1123-1138.

[23]. Khalifa, A., Bashir, B., Çakir, Z., Kaya, Ş., Alsalman, A., and Henaish, A. (2021). Paradigm of Geological Mapping of the Adiyaman Fault Zone of Eastern Turkey Using Landsat 8 Remotely Sensed Data Coupled with PCA, ICA, and MNFA Techniques. ISPRS Int. J. Geo-Inf. 2021.

[24]. El-Qassas, R., Ahmed, S., Abd-ElSalam, H., and Abu-Donia, A. (2021). Integrating of Remote Sensing and Airborne Magnetic Data to Outline the Geologic Structural Lineaments That Controlled Mineralization Deposits for the Area around Gabal El-Niteishat, Central Eastern Desert, Egypt. Geomaterials, 11, 1-21.

[25]. Kamal El-Din., G. M., El-Noby., E., Abdelkareem., M., and Hamimi., Z. (2021). Using multispectral and radar remote sensing data for geological investigation, Qena-Safaga Shear Zone, Eastern Desert, Egypt. Arab. J. Geosci. 14:997.

[26]. Seleim, A.M., Bekiet, M.H., and Hammed., M.S. (2022). Enhanced lithological mapping of Durba-Araba basement blocks, along the eastern margin of the Central Gulf of Suez Rift, Egypt, using Landsat-8 Data. Arabian Journal of Geosciences, 10208. <https://doi.org/10.1007/s12517-022-10208-0>.

[27]. Kröner, A., Krüger, J., and Rashwan, A.A.A. (1994). Age and tectonic setting of granitoid gneisses in the Eastern Desert of Egypt and south-west Sinai. Geol Rundsch, 83:502-513.

[28]. Stern, R.J. (1994). Arc assembly and continental collision in the Neoproterozoic East African orogen: implications for the consolidation of Gondwanaland. Annual Review of Earth and Planetary Sciences, 22: 319-351.

[29]. Stern, R.J. (2002). Crustal evolution in the East African Orogen: a neodymium isotopic perspective. Journal of African Earth Science, 34:109-117.

[30]. Johnson, P.R., Andresen., A., Collins., A.S., Fowler., A.R., Fritz., H., Ghebreab., W., Kusky., T., and Stern., R. J. (2011). Late Cryogenian-Ediacaran history of the Arabian-Nubian Shield: a review of depositional, plutonic, structural, and tectonic event in the closing stages of the northern East African Orogen. J Afr Earth Sci 61:167-232.

[31]. Nasiri Benzenjani, R., Pease, V., Whitehouse, M.J., Shalaby, M.H., Kadi, K.A., and Kozdroj, W. (2014). Detrital zircons geochronology and provenance of the Neoproterozoic Hammamat Group (Igla Basin), Egypt and the Thalbah Group, NW Saudi Arabia: Implications for regional collision tectonics. Precamb Res 245:225-243.

[32]. Basta, F.F., Maurice, A.E., Bakhit, B.R., Azer, M.K., and El-Sobky, A.F. (2017). Intrusive rocks of the Wadi Hamad Area, North Eastern Desert, Egypt: change of magma composition with maturity of

Neoproterozoic continental island arc and the role of collisional plutonism in the differentiation of arc crust. Lithos, Volumes 288-289: 248-263.

[33]. Said, R. (1990). The Geology of Egypt. Balkema, Rotterdam, Brookfield, 730 p.

[34]. Youssef, M.I. (1957). Upper Cretaceous rocks in Kosseir area. Bull. Inst. Desert Egypte 7 (2): 35-54.

[35]. Tarabili, E.E. (1966). General outlines of epeirogenesis and sedimentation in the region between Safaga, Quseir, and southern Wadi Qena area, Eastern Desert, Egypt. American Association of Petroleum Geology Bulletin 50: 1890-1898.

[36]. Abd El-Razik, T.M. (1967). Stratigraphy of the sedimentary cover of the Anz-Atshan-south Duwi district. Bull. Fac. Sci., Cairo Univ. 41: 153-179.

[37]. Said, R. (1962). The Geology of Egypt. Elsevier, Amsterdam-New York, 377p.

[38]. Sadek, A. and Abdel Razik, T.M. (1970). Zonal stratigraphy of the lower Tertiary of Gebel Urn El Huetat Red Sea by means of nannofossils. 7th Arabian Petroleum Congress., Kuwait, Paper 51, 16p.

[39]. Abdel Razik, T.M. (1972). Comparative studies on the upper Cretaceous-early Paleocene sediments of the Red Sea coast, Nile Valley and Western Desert, Egypt. 8th Arab Petroleum Congress., Algiers, B-3, 23p.

[40]. Schrank, E. (1984). Organic-geochemical and palynological studies of a Dakhla Shale profile (late Cretaceous) in southeast Egypt, Part A: Succession of microfloras and depositional environment. Berl. geowiss. abh. reihe a. geol. palaeontol., Berlin. 50: 189-207.

[41]. Khalil, S.M. and Mc Clay, K.R. (2009). Structural control on syn-rift sedimentation, northwestern Red Sea margin, Egypt. Marine and Petroleum Geology, 26, 1018-1034.

[42]. Akkad, S. and Dardir, A.A. (1966). Geology and phosphate deposits of Wasif, Safaga area. Egyptian Geological Survey, Cairo, Paper No.36, 35p.

[43]. El Gezeery, M.N. and Marzouk, I.M. (1974). Miocene rock stratigraphy of Egypt. Egyptian Journal of Geology, 18: 1-59.

[44]. Phillobbos, E.R., El Haddad, A.A., and Mahran, T.M. (1988). Comparison between Miocene and Pliocene facies distribution related to syn-rift tectonics along the Egyptian Red Sea coastal area. Egyptian General Petroleum Corporation, Ninth Petroleum Exploration and Production Conference, 1: 246-254.

[45]. Farahat, E.S., Shehata, A., and Hauenberger, C. (2017). Red Sea rift-related Quseir basalts, central Eastern Desert, Egypt: Petrogenesis and tectonic processes. Bull Volcanol (2017) 79: 9.

- [46]. El Bassyony, A.A. (1982). Stratigraphical Studies on Miocene and Younger Exposures Between Quseir and Berenice, Red Sea Coast, Egypt. PhD thesis, Ain Shams University, Cairo, 200p.
- [47]. Philobos, E.R., El Haddad, A.A., Luger, P., Bekir, R., and Mahran, T.M. (1993). Syn-rift Miocene sedimentation around fault blocks in the Abu Ghusun-Wadi el Gemal area, Red Sea, Egypt. In: Philobos, E.R., Purser, B.H. (eds.), *Geodynamics and Sedimentation of the Red Sea-Gulf of Aden Rift System*. Geological Society of Egypt, Special Publication, 1: 115-142.
- [48]. Orszag-Sperber, F., Purser, B.H., Rioual, M., and Plaziat, J.C. (1998). Post Miocene sedimentation and rift dynamics in the southern Gulf of Suez and northern Red Sea. In: Purser, B.H., Bosence, D.W.J. (eds.), *Sedimentation and Tectonics of Rift Basins: Red Sea-Gulf of Aden*. Chapman and Hall, London, p. 427-447.
- [49]. Sabins, F.F. (2000). *Remote sensing: principles and interpretation* (3rd edition). New York Freeman, New York, 494p.
- [50]. Drury, S.A. (2004). *Image interpretation in geology* (3rd edition), Routledge, Oxfordshire, 304p.
- [51]. Afify, H. A. (2011). Evaluation of change detection techniques for monitoring land-cover changes: a case study in New Burg El-Arab area. *Alexandria Engineering Journal*, 50 (2): 187-195.
- [52]. El Zalaky, M.A., Essam, M.E., and El Arefy, R.A. (2018). Assessment of band ratios and feature-oriented principal component selection (FPCS) techniques for iron oxides mapping with relation to radioactivity using landsat 8 at Bahariya Oasis. *Egypt. Researcher* 10(4):1-10.
- [53]. Jensen, J.R. (1986). *Introductory Digital Image Processing: A Remote Sensing Perspective*, Prentice-Hall, Englewood Cliffs, New Jersey, 379p.
- [54]. Chen, C. H. and Zhang, X. (1999). Independent component analysis for remote sensing study. *Proceedings of SPIE*, 387, 150–158.
- [55]. Gholami., R., Moradzadeh., A., and Yousefi., M. (2012). Assessing the performance of independent component analysis in remote sensing data processing. *J. Indian Soc. Remote Sens.* 40, 577–588.
- [56]. Tempfli, K., Huurneman, G.C., Bakker, W. H., Janssen, L.L.F., Feringa, W.F., Gieske, A.S.M., Grabmaier, K.A., Hecker, C.A., Horn, J.A., Kerle, N., van der Meer, F.D., Parodi, G.N., Pohl, C., Reeves, C.V., van Ruitenbeek, F.J.A., Schetselaar, E.M., Weir, M.J.C., Westinga, E., and Woldai, T. (2009). *Principles of remote sensing: an introductory textbook*. (ITC Educational Textbook Series; Vol. 2). International Institute for Geo-Information Science and Earth Observation. 591p.
- [57]. Continental Oil Company (CONOCO). (1987). *Geological map of Egypt (scale 1:500 000) 1987-1988*. Egypt. Gen. Petrol. Corp. and Conoco, 20 sheets.
- [58]. Khalil, S. and McClay, K. (2001). Tectonic evolution of the northwestern Red Sea-Gulf of Suez rift system. *Geological Society of London, Special Publication* 187, 453-473.
- [59]. Khalil, S.M. and McClay, K.R. (2002). Extensional fault-related folding, northwestern Red Sea, Egypt. *Special Volume. Journal of Structural Geology* 24, 743-762.
- [60]. Khalil, S. and McClay, K. (2018). Extensional fault-related folding in the northwestern Red Sea, Egypt: segmented fault growth, fault linkages, corner folds and basin evolution. *Geological Society of London, Special Publication*, 476, 49-81.
- [61]. Morley, C.K., Nelson, R.A., Patton, T.L., and Munn, S.G. (1990). Transfer zones in the East African Rift System and their relevance to hydrocarbon exploration in rifts. *AAPG Bull.*, 74, 1234-1253.
- [62]. Abdelkareem, M., Akryby, A., Fakhry, M. and Mostafa., M. (2022). Using of remote sensing and aeromagnetic data for predicting potential areas of hydrothermal mineral deposits in the Central Eastern Desert of Egypt. *Journal of Geography and Cartography* (2021) Volume 4 Issue 2, 36-49.
- [63]. Mitchell, A.H.G. and Garson, M.S. (1981). *Mineral deposits and global tectonic setting*. Academic Press, 405pp.
- [64]. Attawiya, M.Y. (1983). Geochemistry and genesis of the uranium mineralization of El Misikat area, Egypt. *Ann. Geol. Surv. Egypt* 13:67-74.
- [65]. Yousefi, M. and Hronsky, J.M.A. (2023). Translation of the function of hydrothermal mineralization-related focused fluid flux into a mappable exploration criterion for mineral exploration targeting. *Applied Geochemistry* 149 (2023) 105561.

اجرای تکنیک‌های سنجش از دور در نقشه‌برداری ساختاری و سنگ‌شناسی حاشیه شمال غربی دریای سرخ،

مصر

فاروق سید^{۱*}، محمد حامد^۲، احمد شید^۱ و احمد حسین^۱

۱. گروه زمین‌شناسی، دانشکده علوم، دانشگاه فیوم، مصر

۲. گروه زمین‌شناسی، دانشکده علوم، دانشگاه قاهره، مصر

ارسال ۲۰۲۲/۰۱/۲۱، پذیرش ۲۰۲۳/۰۳/۱۸

* نویسنده مسئول مکاتبات: Fsm00@fayoum.edu.eg

چکیده:

حاشیه شمال غربی دریای سرخ به صورت چندین بلوک گسلی مرتبط با شکاف توسعه یافته است. این بلوک‌های گسلی شامل دو ابر تکتونو چینه‌ای است. توالی پیش شکاف را می‌توان به سنگ‌های زیرزمین پرکامبرین و نهشته‌های ائوسن کرتاسه بالایی-پایینی تقسیم کرد، در حالی که توالی سین-شکاف شامل نهشته‌های الیگوسن تا کواترنر است. تمایز سنگ‌شناسی این واحدهای سنگی که در منطقه مورد مطالعه با آن مواجه می‌شوند، با استفاده از تکنیک‌های مختلف تقویت تصاویر سنجش از دور داده‌های OLI (Landsat-8) با کمک راستی‌آزمایی میدانی انجام می‌شود. تجزیه و تحلیل امضای طیفی واحدهای سنگی مختلف، کامپوزیت رنگ کاذب، نسبت باند، تجزیه و تحلیل اجزای اصلی، کسر نویز حداقل، و تجزیه و تحلیل اجزای مستقل ابزارهای قدرتمندی در تشخیص واحدهای سنگ اصلی هستند. تکنیک طبقه‌بندی نظارت بر فاصله حداکثر احتمال ابزاری قوی است. در شناسایی تماس بین واحدهای سنگی مختلف. داده‌های DEM تصحیح شده زمین (RTC) استخراج شده از PALSAR با وضوح فضایی ۱۲/۵ متر برای ساخت یک تصویر نمای پرسپکتیو سه‌بعدی از منطقه مورد مطالعه استفاده می‌شود. مطالعه حاضر یک روش منحصر به فرد برای تشخیص سنگ‌شناسی واحدهای سنگ اصلی با استفاده از تصاویر OLI ارائه می‌کند و یک نقشه ساختاری با وضوح بالا از منطقه مورد مطالعه را با کمک راستی‌آزمایی میدانی معرفی می‌کند.

کلمات کلیدی: Landsat-8 (OLI)، PALSAR، تکنیک‌های سنجش از دور، نقشه برداری ساختاری، دریای سرخ.